



Wind tunnel study on natural instability of the normal force on a full-scale wind turbine blade section at Reynolds number 4.7×10^6

Ingrid Neunaber, Frédéric Danbon, Antoine Soulier, Dimitri Voisin,
Emmanuel Guilmineau, Philippe Delpech, Sébastien Courtine, Claire
Taymans, Caroline Braud

► To cite this version:

Ingrid Neunaber, Frédéric Danbon, Antoine Soulier, Dimitri Voisin, Emmanuel Guilmineau, et al.. Wind tunnel study on natural instability of the normal force on a full-scale wind turbine blade section at Reynolds number 4.7×10^6 . Wind Energy, 2022, 25 (8), p. 1332-1342. 10.1002/we.2732 . hal-03862699

HAL Id: hal-03862699

<https://hal.science/hal-03862699>

Submitted on 21 Nov 2022


HAL is a multi-disciplinary open access archive for the deposit and dissemination of scientific research documents, whether they are published or not. The documents may come from teaching and research institutions in France or abroad, or from public or private research centers.

L'archive ouverte pluridisciplinaire **HAL**, est destinée au dépôt et à la diffusion de documents scientifiques de niveau recherche, publiés ou non, émanant des établissements d'enseignement et de recherche français ou étrangers, des laboratoires publics ou privés.

RESEARCH ARTICLE

WILEY

Wind tunnel study on natural instability of the normal force on a full-scale wind turbine blade section at Reynolds number $4.7 \cdot 10^6$

Ingrid Neunaber¹  | Frédéric Danbon² | Antoine Soulier³ | Dimitri Voisin³ | Emmanuel Guilmineau¹ | Philippe Delpech² | Sébastien Courtine² | Claire Taymans⁴ | Caroline Braud^{1,2}

¹LHEEA Laboratory, Centrale Nantes/CNRS, Nantes, France

²CSTB, Nantes, France

³Mer Agitée, Port-La-Forêt, France

⁴Valemo, Bégles, France

Correspondence

Ingrid Neunaber, CSTB, 1 Rue de la Noë, 44321 Nantes, France.

Email: ingrid.neunaber@uol.de

Funding information

Pays-de-Loire, Centrale Nantes, CSTB, and Ville de Nantes, Grant/Award Number: 2018 ASAPe; ADEME/region Pays-de-Loire, Grant/Award Number: 1905C0030

Abstract

Wind turbines are exposed to the turbulent wind of the atmospheric boundary layer. Consequently, the aerodynamic forces acting on the rotor blades are highly complex. To improve the understanding, a common practice is the experimental or numerical investigation of 2d (wind turbine) blade sections. In these investigations, the flow around the 2d blade section is assumed to be two-dimensional; however, 3d effects are known to occur. Therefore, we combine 2d CFD simulations and experimental investigations in a wind tunnel with a 2d wind turbine rotor blade section at full-scale (i.e., chord length $c = 1.25\text{m}$ and chord-based Reynolds number of $Re_c = 4.7 \cdot 10^6$). In the wind tunnel, the inflow turbulence intensity is $TI \approx 1.5\%$. To avoid wall effects biasing the results, the profile does not span the whole test section. The profile was equipped with two rows of pressure taps around the airfoil, close to the center, to monitor the time-resolved aerodynamic response as well as the flow around the airfoil. The normal force, c_p curves, and the separation point are analyzed. While 2d simulations and experiments match well, in the experiments, we find natural instabilities, that is, local and temporal variations of the flow separation point at angles of attack close to the maximum lift that are not triggered externally, for example, by inflow variations.

KEYWORDS

3d effects, unsteady aerodynamics, wind energy, wind tunnel experiments

1 | INTRODUCTION

For decades, the prediction and the manipulation of blade aerodynamic forces have been of high interest in the field of wind energy to improve the stall margin in the design process of wind turbines, alleviate loads, decrease noise impacts, increase the blade life-time, and increase the power during operation. Starting from aerodynamic profiles used in aviation, the rotor blades used in today's wind turbines are highly specialized, and their shapes are adapted to the turbulent environment. With very large offshore wind turbines subjected to inflow wind with local shears over their rotor-sweep area, knowledge of the aerodynamics at the rotor blade is becoming even more essential. Also, offshore wind turbines are

This is an open access article under the terms of the [Creative Commons Attribution-NonCommercial-NoDerivs](https://creativecommons.org/licenses/by-nc-nd/4.0/) License, which permits use and distribution in any medium, provided the original work is properly cited, the use is non-commercial and no modifications or adaptations are made.

© 2022 The Authors. *Wind Energy* published by John Wiley & Sons Ltd.

operating in dense farm layouts where the wakes of upstream wind turbines interact with following lines of rotors and may induce additional load fluctuations.¹

Good knowledge of the blade aerodynamics in complex environments becomes more and more crucial. Therefore, experiments have been carried out on large, highly equipped wind turbine models in wind tunnels (e.g., within the IEA task 29²) and on highly equipped full-scale wind turbines in operation (e.g., Schaffarczyk et al.³ and Madsen et al.⁴). While these experimental campaigns helped significantly to advance the knowledge of the blade aerodynamics, there are still a lot of open questions because of the complexity of these investigations. For example, translating results obtained using 3d rotors in the wind tunnel faces the difficulty of far lower chord-based Reynolds numbers which influences the boundary layer (BL) on the airfoil's surface and, thus, the aerodynamic performance. In field experiments, the investigation of the blade aerodynamics at full-scale turbines proves to be difficult. For example, the inflow conditions are highly instationary and often unexplored or lacking detail. Therefore, to help advance with the open questions, numerical and experimental investigations of 2d blade sections in uniform inflow and without rotation are often used as an alternative to 3d experimental campaigns.

While a large number of (wind turbine) profile families is available for selection in order to carry out aerodynamic investigations, the aerodynamic profiles used for the rotor blades are usually customized by the manufacturer and, thus, unknown. This complicates both aerodynamic investigations and finding optimal positions when equipping the rotor blades of a turbine with aerodynamic sensors. One possibility to obtain the profile shape is by scanning the rotor blade of a wind turbine, which was for example done in Balaesque et al.⁵ for an investigation of “the potential of possible enhancement of energy yield by improving the aerodynamic performance” and Krog Kruse et al.⁶ to include leading edge damage and erosion altering the rotor blade over time.

In investigations of 2d blade sections, the flow effects are assumed to be two-dimensional. However, the lift and drag forces acting on 2d blade sections are known to be sensitive to different parameters such as the blade geometry, the turbulence intensity in the inflow, the Reynolds number, dynamic changes of the angle of attack, or surface roughness elements. While this is particularly true at angles of attack close to the angle of maximum lift, it should be mentioned that an influence of roughness elements and the turbulence intensity of the inflow on the laminar-to-turbulent transition of the flow around the airfoil can also be observed already at low angles of attack (cf. other studies,^{7–9} respectively). An example for 3d flow effects at angles of attack close to the maximum lift can be found in Manolesos and Papadakis¹⁰ where simulations of the flow across a 2d flatback wind turbine airfoil have been compared for different aspect ratios at angles of attack close to the maximum lift. In this paper and the literature review, we, too, will focus on experimental studies of the aerodynamic behavior at angles of attack close to the maximum lift.

At angles of attack close to the maximum lift, early studies have investigated the occurrence of stall depending on the airfoil geometry^{*} and the Reynolds number.¹¹ They found four types of stall in total, inter alia the *trailing edge stall* with gradual and continuous force and momentum variations that is characterized by a well-rounded lift-curve peak, and the *combined trailing edge and leading edge stall* that is shown by either a semi-rounded lift-curve peak followed by an abrupt decrease, or a relatively sharp lift-curve peak followed by a relatively rapid decrease. It should be noted that the term “stall” is employed in these studies even if the flow separation occurs only close to the trailing edge but has not yet reached the leading edge.

The impact of the turbulence intensity in the inflow on the aerodynamics of a 2d blade section has been investigated in different works and an overview on different studies can be found in Li and Hearst¹² where the impact of different turbulence levels up to 5.4% on the aerodynamics of a NREL S826 profile was investigated for a chord-based Reynolds number of $Re_c = 4 \cdot 10^5$. $Re_c = \frac{c \cdot u}{\nu}$, where c denotes the chord length, u denotes the inflow velocity, and ν the kinematic viscosity. They found that an increase of the turbulence intensity increases the slope of the linear part of the lift curve. Also, turbulence intensities of up to 1.6% were associated with a reduction of the maximum lift, whereas turbulence intensities of 2.1% and higher were associated with an increase in lift compared to the reference case. Near the maximum lift angle of attack, Devinant et al.¹³ and Sicot et al.¹⁴ have examined the impact of turbulence intensities up to 16% on the aerodynamics of a 2d NACA65(4)421 blade section at chord-based Reynolds numbers $1 \cdot 10^5 \leq Re_c \leq 7 \cdot 10^5$. Devinant et al.¹³ show that the stall angle is shifted towards higher angles of attack with increasing the turbulence intensity. The authors attribute this to a displacement of the transition towards the trailing edge due to a turbulent BL flow that is known to be less prompt to flow separation. Sicot et al.¹⁴ show an increase of the standard deviation of the surface pressure measurements in the separated flow region with increasing turbulence intensity, while the average location of the separation line remains unchanged.

In recent collaborative wind tunnel experiments presented by Olsen et al.,¹⁵ the high sensitivity of the lift curve close to the maximum lift to small differences in the experimental execution has been demonstrated. In this study and in Krog Kruse et al.,⁶ lift curves were measured in four different wind tunnels (Poul La Cour tunnel at DTU's Risø campus, Delft University of Technologie, LM Wind Power, and University of Stuttgart) under similar conditions (low-turbulent inflow (<0.1%), $Re_c = 3 \cdot 10^6$) using 2d blade sections of type NACA63-418. Despite these similarities, results exhibit a large dispersion of the lift curve around its maximum value. While different aspect ratios, slightly different turbulence levels, and different blockage ratios are given as possible explanations by the authors, they also suspect the use of different measurement techniques to extract the lift forces as one main reason.

*The airfoil geometries investigated were improved for aeronautic applications rather than wind energy applications.

At different operating wind turbines equipped with rotor blades of the NACA63-2nn or NACA63-4nn airfoil series, Bak et al.¹⁶ reported the occurrence of combined trailing edge and leading edge stall. They were able to reproduce this phenomenon using a 2d NACA63-215 blade section in wind tunnel experiments in uniform inflow at chord-based Reynolds numbers of $Re_c \geq 1 \cdot 10^6$. The combined trailing edge and leading edge stall observed at maximum lift induces two stable branches on the lift curve. The upper branch of the lift curve corresponds to a trailing edge flow separation, whereas the lower branch of the lift curve corresponds to a flow that separates at the leading edge and over the whole suction side of the blade surface. By means of computational fluid dynamics simulations, the authors relate this sudden shift in the lift to the bursting of the laminar separation bubble at the leading edge of the airfoil. In different studies, Manolesos et al.^{17,18} and Ragni et al.¹⁹ have demonstrated three-dimensional flow separation at 2d blade sections in wind tunnel experiments at chord-based Reynolds numbers of $O(10^6)$ and low turbulence intensities. A span-wise distribution of stall cells near the maximum lift value was verified.

Overall, this demonstrates that the flow around an airfoil is highly sensitive at angles of attack close to the maximum lift, even in experiments using 2d airfoils. Conclusions may be biased because the flow becomes three-dimensional at angles of attack near the maximum lift, which can impact results depending on the use of global measurement techniques such as aerodynamic balances or tunnel wall pressures, or very local measurements as for example a single pressure crown at the centerline of the blade section.

In this study, we carry out an experiment designed to improve knowledge of the aerodynamic behavior of a wind turbine blade section. To include possible 3d flow effects, local measurements at two span-wise positions are done at a realistic chord-based Reynolds number.

Particularly, two *research questions* arise from the lack of local, temporally resolved measurements of the flow around 2d blade sections around angles of attack close to the maximum lift:

1. Do spatial variations of the flow occur?
2. Do temporal variations of the flow occur?

We address these questions by means of the following *research objectives*:

- Aerodynamic measurements at a 2d blade section with an original (i.e., not scaled down) chord length of 1.25m that is used at a 2-MW wind turbine at 80% of the radius; the Reynolds number is $Re_c = 4.7 \cdot 10^6$ and an inflow with $u_0 = 55.6 \text{ ms}^{-1}$ and $TI \approx 1.5\%$ is used.
- Spatial and temporal resolution of the flow around the 2d blade section using two chord-wise rows of dynamic differential pressure sensors
- Comparison of the measurement data with 2d CFD simulations

The experiments presented here are partially carried out in preparation for a field campaign within the research project ePARADISE. This project aims at equipping a rotor blade of an operated wind turbine with sensors, and to find the best positions of these sensors, the aerodynamic behavior of the blade section at the radial position where they will be positioned needs to be known. The special features of this experimental campaign include the use of a highly equipped 2d blade section of original size whose shape was derived by scanning a real wind turbine blade and the field-value chord-based Reynolds number of $Re_c = 4.7 \cdot 10^6$ which made the use of a very large experimental facility necessary.

In the following, the methodology is described, giving details on the 2d blade section, the measurements, and the simulations. Afterwards, the results are presented, and finally, a conclusion discusses and summarizes the main results.

2 | METHODOLOGY

In the following, the methodology used to investigate the high sensitivity of the aerodynamic behavior will be introduced. First, the 2d blade section is presented, then the experimental setup is shown, and afterwards, the simulations are explained. Finally, the data evaluation is briefly indicated.

2.1 | 2d blade section

In Figure 1, the 2d blade section that was used during the experiments and the simulations is shown. The shape of the profile was derived by scanning the blade of a 2-MW commercial wind turbine operated by VALEMO at the Saint-Hilaire de Chaléons site in France. The extracted 2d blade section is located at 80% of the rotor radius. While we are aware that the profile shape is customized and may therefore not be from the NACA series, to give the reader an idea of a similar profile, we would like to show a comparison with the NACA63-3-420 airfoil geometry but with a higher camber of 4% instead of 2%. According to the study of Gault,¹¹ who investigated the stall types of 150 different 2d airfoil shapes with thicknesses mostly around 10% to 12%, the present scanned blade profile is expected to have either a trailing edge stall or a combined trailing edge and leading edge stall behavior.

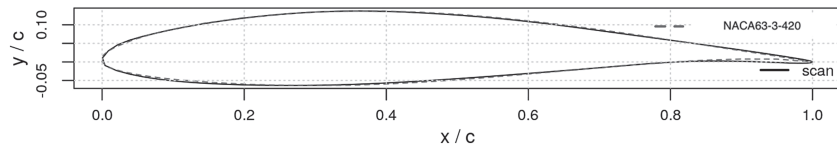


FIGURE 1 Cross-section of the rotor blade at 80% of the radius in comparison with a NACA63-3-420 profile with a modified camber of 4% instead of 2%

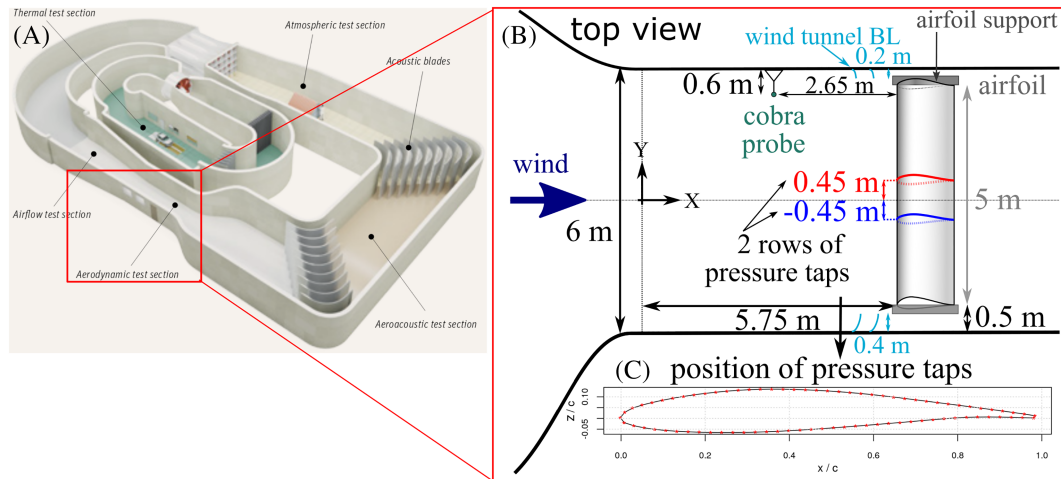


FIGURE 2 Setup: The measurements were performed in the aerodynamic test section of the Jules Verne Climatic Wind Tunnel at CSTB (A). A 2d blade section was installed in the test section (B), and it is equipped with two rows of 78 pressure taps each (C). The inflow is measured 2.65m upstream of the profile by a cobra probe

From the derived profile shape, a mock-up was built for the experimental investigation. The final 2d blade section is 5m wide and has the original, that is, not scaled, chord length of $c = 1.25\text{m}$. The aspect ratio is thus 4.

2.2 | Setup

The experiments that we present here were carried out in the aerodynamic test section of the Jules Verne Climatic Wind Tunnel at CSTB, compare Figure 2A. The inlet is 6m wide and 5m high, and the test section has a length of 12m. Wind speeds up to 70ms^{-1} can be reached, and the wind speed is kept constant by a control that takes into account air density variations. The flow uniformity and the turbulence intensity were characterized before the measurements. The velocity profile across the test section was measured using several cobra probes sampled at 1024Hz. The measurement duration was 2 min. Six-meter downstream of the inlet, eight velocities ranging from 6 to 43ms^{-1} were investigated in steps of 0.5m at a height of 1.2m. For velocities larger than 6ms^{-1} , the turbulence intensity varies between 1.3% and 1.7% independently of the inflow velocity, and the span-wise variations of the mean velocity are around 1% to 2%. Therefore, homogeneity of the flow is given for the mean velocity. The turbulence intensity increases towards the inner side of the wind tunnel (i.e., $Y < 0$) up to 1.5m from the wall, caused by the history of the flow in the return circuit, and the variations are around 10%. Additionally, the BLs on the ground, ceiling, and both sides were studied carefully for seven velocities ranging from 12 to 54ms^{-1} in the middle of the test section. The BL height is about 30cm on the ground, 25cm on the ceiling, about 18cm on the outer side (i.e., $Y > 0$) and between 30 and 40cm on the inner side (i.e., $Y < 0$, where the turbulence level is also higher). The wind tunnel BLs at the walls are also indicated in Figure 2B. Finally, a spectral analysis was performed that allows to exclude the presence of abnormal coherent structures at a given size (i.e., peaks in the spectrum) in the flow in the test section.

The 2d blade section introduced in Section 2.1 was installed 5.75m from the inlet on a support structure that allowed to set pre-defined angles of attack α . With a width of 5m, it is not spanning the whole width of the test section to avoid interactions with the wind tunnel BLs. While no end plates were installed at the model, nylon tufts were installed at both sides of the blade section and in the centerline. This helps to locate the extend of vortices forming at the profile ends in correlation of what happens in the centerline. It was found that an influence can be seen in the first 50cm in span-wise direction at both sides of the blade section, but it never reaches the centerline and it is far from the span-wise locations of the two wall pressure lines described below.

To measure the differential pressure, the 2d blade section is equipped with two rows of 78 uniformly spaced pressure taps around the airfoil located at $Y_m = -450$ mm and $Y_p = 450$ mm from the wind tunnel center, compare Figure 2B,C. The chord-wise spacing between the pressure taps is $0.026c$. The pressure taps are connected to five multiplexed EPS pressure scanners of 32 channels each, using of 1.5 meter vinyl tubes with an internal diameter of 0.8mm. The range of the pressure sensors is $0 \leq 2.5$ kPa with a precision of $\pm 0.03\%$ of the full measurement range. The transfer function of the whole system (tubes plus sensor cavity) has been measured off-line at a sampling frequency of $f_s = 1024$ Hz (for the methodology, see, e.g., Holmes & Lewis²⁰ and Whitmore et al.²¹). The cut-off frequency is approximately 200 Hz. The signal acquisition is performed using two National Instrument acquisition boards linked by real-time system integration for synchronization purposes. During the measurements, the sampling frequency was $f_s = 400$ Hz. During post-processing, the inverse transfer function is applied to the raw signals before the analysis. In addition to these profile surface pressure measurements, the dynamic pressure q_0 was measured above the 2d blade section (at the same downstream location) using a Pitot tube.

Measurements were carried out at 13 angles of attack between $\alpha = -10^\circ$ and $\alpha = 24^\circ$. The maximum wind tunnel blockage at $\alpha = 24^\circ$ is 13.5% (10% blockage from the profile and 3.5% blockage from the support structure). The measurement duration was 120 s for each angle of attack. A comparison of the results from the two sensor rows will indicate whether the flow around the center of the 2d blade section is 2d or whether 3d flow phenomena occur.

The inflow velocity was $u_0 = 55.6$ ms⁻¹ which is equal to a chord-based Reynolds number of $Re_c = 4.7 \cdot 10^6$. A cobra probe installed 2.65-m upstream of the airfoil was used to measure the velocity alongside the pressure, and the cobra probe was sampled with $f_{s,c} = 500$ Hz.

2.3 | Simulations

The ISIS-CFD flow solver, developed by Centrale Nantes and CNRS, uses an incompressible unsteady Reynolds-averaged Navier–Stokes (URANS) method. The solver is based on a finite volume method to build the spatial discretization of the transport equations. The unstructured discretization is face-based, which means that cells with an arbitrary number of faces are accepted. A second-order backward difference scheme is used to discretize time. The solver can simulate both steady and unsteady flows. In the case of turbulent flows, additional transport equations for the variables in the turbulence model are added. All flow variables are stored at the geometric center of arbitrary shaped cells. Volume and surface integrals are evaluated with second-order accurate approximations. Numerical fluxes are reconstructed on the mesh faces by linear extrapolation of the integrand from the neighboring cell centers. The velocity field is obtained from the momentum conservation equations while the pressure field is extracted from the mass conservation constraint or continuity equation, transformed into a pressure equation. The pressure equation is obtained by the Rhie and Chow interpolation technique.²² The momentum and pressure equations are solved in a segregated manner as in the SIMPLE coupling procedure.²³

A two-dimensional simulation has been carried out using the 2d blade section presented in Section 2.1 for angles of attack between -10° and 16° . The turbulence model used is $k-\omega$ SST,²⁴ and no transition model was used. These simulations are unsteady simulations. The value of the time step is $\Delta t U_\infty / c = 0.01$, and for each time step, a reduction by two orders of magnitude of nonlinear residuals of discrete momentum equation is carried out. The mesh is using Hexpress™, an automatic unstructured mesh generator. This software generates meshes containing only hexahedrals. A mesh convergence study has been performed. Table 1 gives details about the meshes used. For all meshes, the maximum value of y^+ is 0.8, and the average value is 0.3. The results for the angle of attack $\alpha = 14^\circ$ in Table 2 shows that mesh convergence is achieved for the drag coefficient C_D and the lift coefficient C_L . The error between the “medium” and “fine” meshes is small enough to be acceptable. For the rest of the study, the “medium” mesh will be used. For this mesh, up to a distance of $0.005 \times c$ from the profile, the stretch ratio is 1.2. After this distance,

TABLE 1 Information on the three meshes used

Mesh	Nb of nodes	Nb of cells	Nb of cells on the airfoil
Coarse	140,310	138,648	974
Medium	234,324	232,113	1292
Fine	352,772	350,006	1614

TABLE 2 Grid independence study for the angle of attack $\alpha = 14^\circ$

Mesh	C_D	C_D error	C_L	C_L error
Coarse	0.0267	16.8%	1.5191	−4.1%
Medium	0.0325	−1.2%	1.4515	0.6%
Fine	0.0321	—	1.4600	—

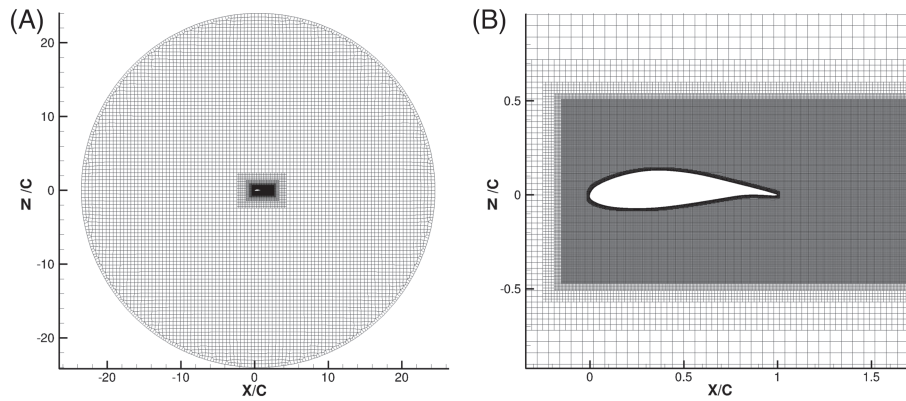


FIGURE 3 View of the mesh used for the simulations: (A) General view and (B) zoomed view from (A)

the cells are isotropic and have a size of $0.001 \times c$ up to $0.019 \times c$ from the profile. Then, in a box starting $0.12 \times c$ in front of the profile and extending to $1.48 \times c$ past the profile, the cells are isotropic and have a size of $0.038 \times c$. Figure 3 presents a view of this mesh.

2.4 | Evaluation of the data

In this study, we will primarily investigate the normal force coefficient c_N and the pressure coefficient $c_p = \Delta p / q_0$ (with Δp the differential pressure and q_0 the dynamic pressure). The normal force coefficient indicates the normal force acting on the airfoil in the airfoil coordinate system, and it can be derived by integrating the pressure coefficient around the airfoil. As the lift force is calculated from the normal and tangential forces, and the latter are only partially retrievable from the pressure coefficient,[†] we will focus on the normal force coefficient in this study. The flow separation point was derived by identifying an increase of the derivative dc_p/dX of the c_p curves over a threshold of 1, a criterion that was found to give good results.

3 | RESULTS

In the following, the results will be presented focusing on the two research questions formulated in the introduction. We start with the investigation of the normal force coefficient as a global quantity. This is followed by an analysis of the local flow behavior, discussing the mean chord-wise pressure distributions at the two span-wise measurement locations together with the time-resolved separation point and the instantaneous pressure at isolated chord-wise positions.

3.1 | Normal force coefficient

In Figure 4A, the mean normal force coefficient is plotted over the angle of attack in the case of the two span-wise measurement positions and the simulations. The symbols represent mean c_N at Y_m (squares) and Y_p (circles) while small dots around the symbols (visible in the zoom in Figure 4A) represent variations of the normal force values for a one second average signal.

A clear asymmetry of c_N measured at the span-wise positions Y_m and Y_p can be observed between $\alpha = 12^\circ$ and $\alpha = 16^\circ$. The maximum normal force differs for the two positions and is reached at different α . As the dots indicate temporal fluctuations of c_N at $\alpha = 14^\circ$, the instantaneous c_N (averaged over 1s) is plotted in Figure 4B. More fluctuations are found at Y_m as compared to Y_p , indicating a more turbulent activity of the flow at the span-wise Y_m position. The evolution of the normal force at Y_m can be associated with flow separation from the airfoil surface at the leading or trailing edge, whereas the evolution of the normal force at Y_p is closer to a flow configuration attached on the suction side of the airfoil. Clearly, the flow across the airfoil shows 3d flow behavior that is stationary. As the simulations follow the upper branch of the normal force coefficient, it can also be concluded that the Y_p curve exhibits a similar behavior as obtained by 2d flow simulations.

Figure 4C shows the instantaneous c_N (averaged over 1s) at $\alpha = 16^\circ$. While the mean normal force coefficient is similar for both span-wise measurement positions, the investigation of the instantaneous c_N reveals first, that an asymmetry of the c_N , and thus the flow around the 2d blade

[†]The viscous part of the tangential force is ignored using this measurement method.

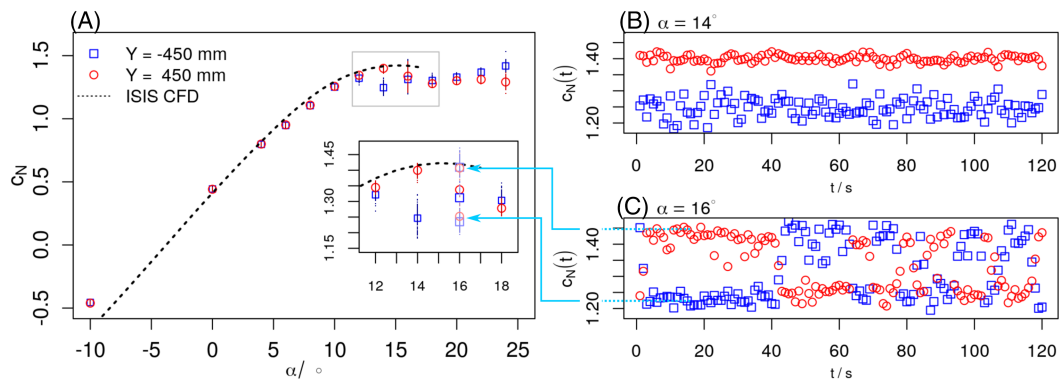


FIGURE 4 (A) Normal force coefficient: Comparison of the measurements at $Y_m = -450$ mm (blue squares), $Y_p = 450$ mm (red circles) and CFD simulations (black dashed line). In addition, the variations of the temporally resolved calculations of c_N are indicated as small dots for the measurements. (B) Evolution of the normal force over time for $\alpha = 14^\circ$. (C) Evolution of the normal force over time for $\alpha = 16^\circ$

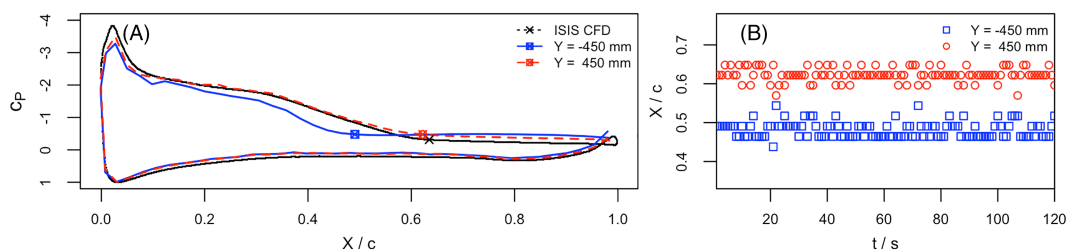


FIGURE 5 (A) Comparison of the c_p distributions at $\alpha = 14^\circ$ and $Re = 4.71 \cdot 10^6$ for the measurements at $Y_m = -450$ mm (blue line), $Y_p = 450$ mm (red dashed line) and CFD simulations (black dots). The separation point is marked in addition for each curve. (B) Fluctuation of the separation point during the measurements

section, is present. Second, we observe that the state is not stable anymore as it was at $\alpha = 14^\circ$, but that the normal force measured at the two positions is alternating reciprocally between two states. We therefore find a clear indication of a bi-stable flow state with an indication of a spatio-temporal correlation between the pressure signals at Y_m and Y_p . The two states of the normal force at $\alpha = 16^\circ$ are added in the zoom in Figure 4A.

The lower branch of the normal force at $\alpha = 14^\circ$ and the bi-stable state at $\alpha = 16^\circ$ are likely consequences of a transition towards an instationary 3d flow organization starting near the maximum lift. For $\alpha > 16^\circ$, the dots indicating the temporal fluctuations of c_N , Figure 4A, do not show large variations. A clear bi-stable flow is only found at $\alpha = 16^\circ$. However, another asymmetry is found at $\alpha \geq 22^\circ$. It grows with increasing α , and the normal force is inverted as compared to the asymmetry at $\alpha = 14^\circ$.

3.2 | c_p distribution and separation point

To investigate the behavior of the flow around the airfoil in detail, we will discuss the pressure distribution in the following. Figure 5A shows the c_p distribution around the 2d blade section at $\alpha = 14^\circ$ for both measurement positions and the numerical results. At this α , a spatial asymmetry of the normal force was observed in the lift curve, and we can assign this to a difference in the trailing edge flow separation location at Y_m and Y_p : At Y_m , the trailing edge flow separation, marked by a blue crossed square, starts at $X/c \approx 0.47$ and thus closer to the leading edge than at Y_p (red crossed circle), where it starts at $X/c \approx 0.63$. A comparison of the results with the simulations suggests that the pressure distribution at Y_p exhibits a similar behavior as obtained by the 2d flow simulations. The difference between Y_m and Y_p indicates that 3d flow separation as observed by Manolesos et al¹⁸ may occur, leading to a larger separation region. However, further investigations are needed to conclude on that point. The investigation of the location of the instantaneous separation point plotted in Figure 5B is stable with only little displacement around its mean value, verifying the asymmetric behavior of the flow around the airfoil.

Figure 6A shows how the mean c_p curves collapse at $\alpha = 16^\circ$ for both measurement positions and that the location of the mean separation point is similar. However, when looking at the fluctuations of the separation point of the 1-s average data, compare Figure 6B, it is obvious that the separation points are not identical. One separation point is located at $X/c \approx 0.42$ while the other one is located at $X/c \approx 0.55$. A reciprocal alternation between the two states is observed at the two span-wise measurement locations. The bi-stability already seen in the normal force

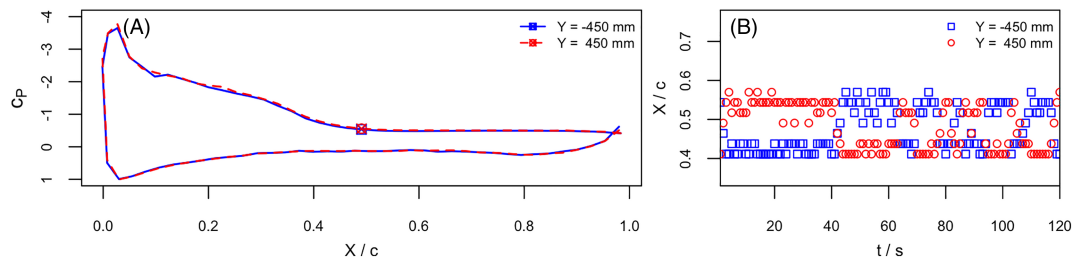


FIGURE 6 (A) Comparison of the c_p distributions at $\alpha = 16^\circ$ and $Re = 4.71 \cdot 10^6$ for the measurements at $Y_m = -450$ mm (blue line) and $Y_p = 450$ mm (red dashed line). The separation point is marked in addition for each curve. (B) Fluctuation of the separation point during the measurements

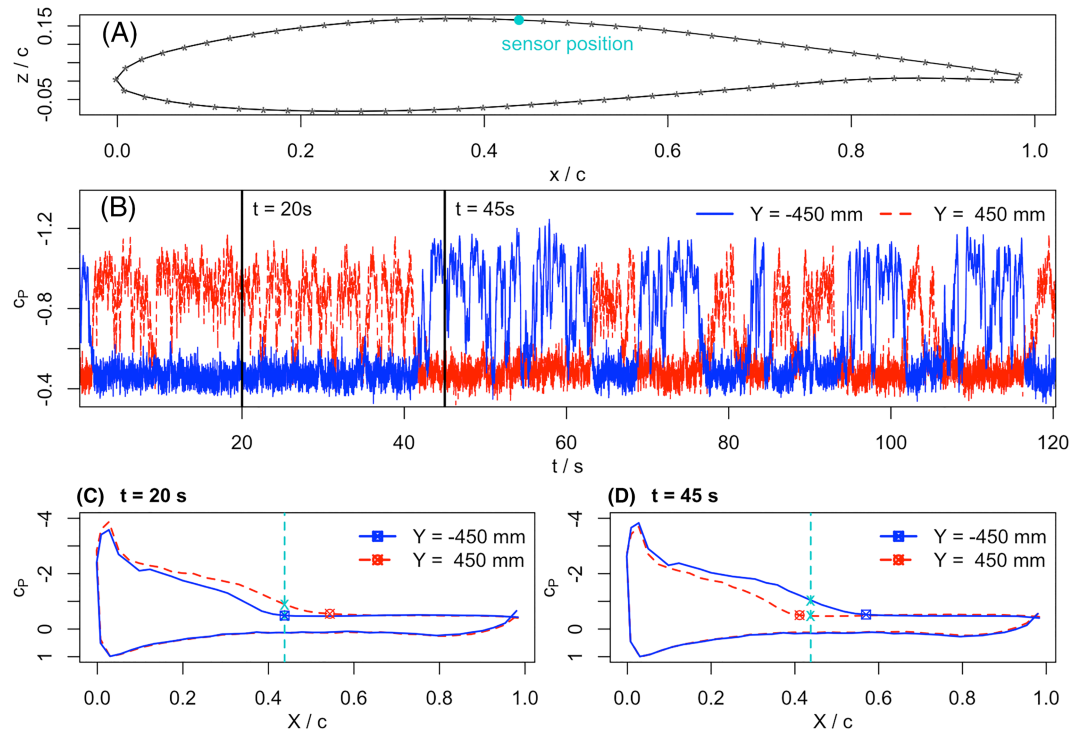


FIGURE 7 (A) Indication of the sensor position used in plot (B). (B) Time series of the c_p at $\alpha = 16^\circ$ and $X/c \approx 0.44$ for the two different sensor positions Y_p and Y_m . (C) c_p distribution at $t = 20$ s—the vertical line marks the sensor position for plot (B). (D) c_p distribution at $t = 45$ s—the vertical line marks the sensor position for plot (B)

coefficient, compare Figure 4C, is therefore clearly associated with sudden displacements of the separation point in time, and we see spatio-temporal correlations.

To further investigate the link between the bi-stable separation point at $\alpha = 16^\circ$ and the pressure fluctuations, the time series of two pressure sensors at Y_p and Y_m , located at the suction side at $X/c \approx 0.44$, are plotted in Figure 7B. The position of the sensor is indicated in Figure 7A. We observe the reciprocal alternation pattern of the bi-stable state that was already shown in the investigation of the 1 s-average c_N and separation point, which indicates a spatio-temporal correlation occurring despite a uniform inflow. The chord-wise position of the pressure sensors was chosen to be between the two separation points of the bi-stable state, so that a single sensor position is sufficient to capture this phenomenon. This is particularly interesting for blade monitoring purposes.

Finally, to show that this phenomenon of the reciprocal alternation pattern of the bi-stable state is restricted to a very small range of angles of attack, Figures 8 and 9 indicate the c_p distribution, (A), and the fluctuations of the separation point, (B), at $\alpha = 18^\circ$ and $\alpha = 24^\circ$, respectively. Additionally, the time series of two pressure sensors at Y_p and Y_m located approximately at the separation point location are shown in (C). In contrast to $\alpha = 14^\circ$ and $\alpha = 16^\circ$, the separation point neither fluctuates as much nor can any correlation between the fluctuations be identified. At $\alpha = 24^\circ$, a bi-stability is visible again, but, as mentioned before, without correlated fluctuations of the separation point.

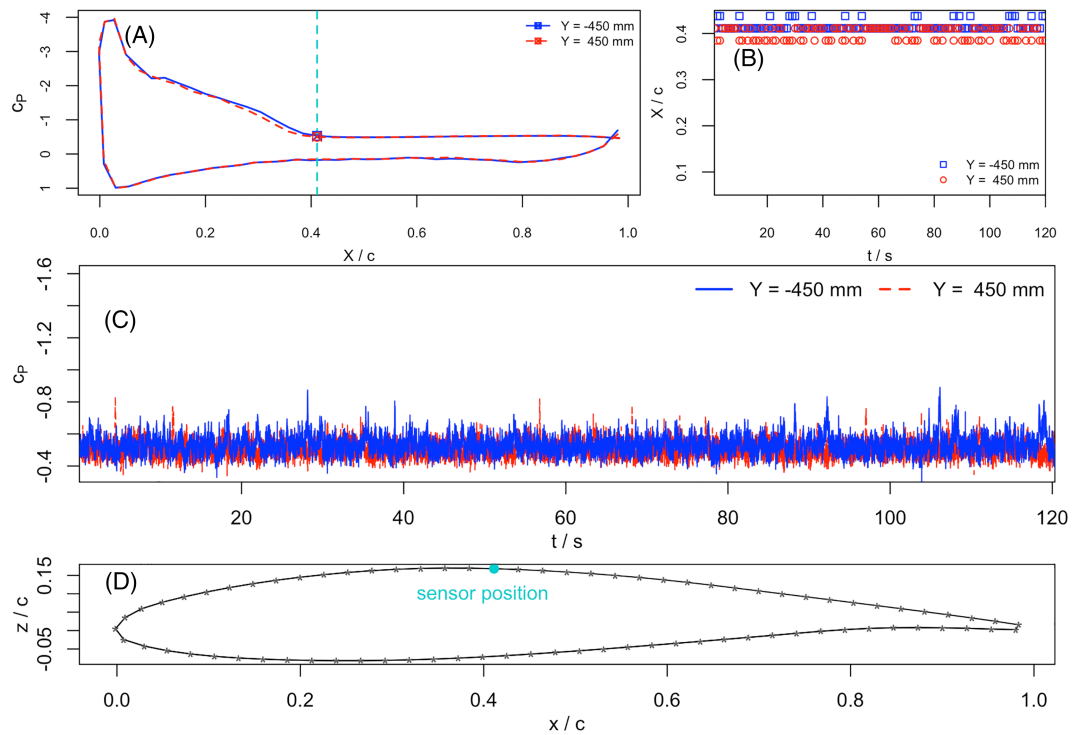


FIGURE 8 (A) Comparison of the c_p distributions at $\alpha = 18^\circ$ and $Re = 4.71 \cdot 10^6$ for the measurements at $Y_m = -450$ mm (blue line) and $Y_p = 450$ mm (red dashed line). The separation point is marked in addition for each curve. (B) Fluctuation of the separation point during the measurements. (C) Exemplary time series of a sensor (marked in D) located around the position of the separation point

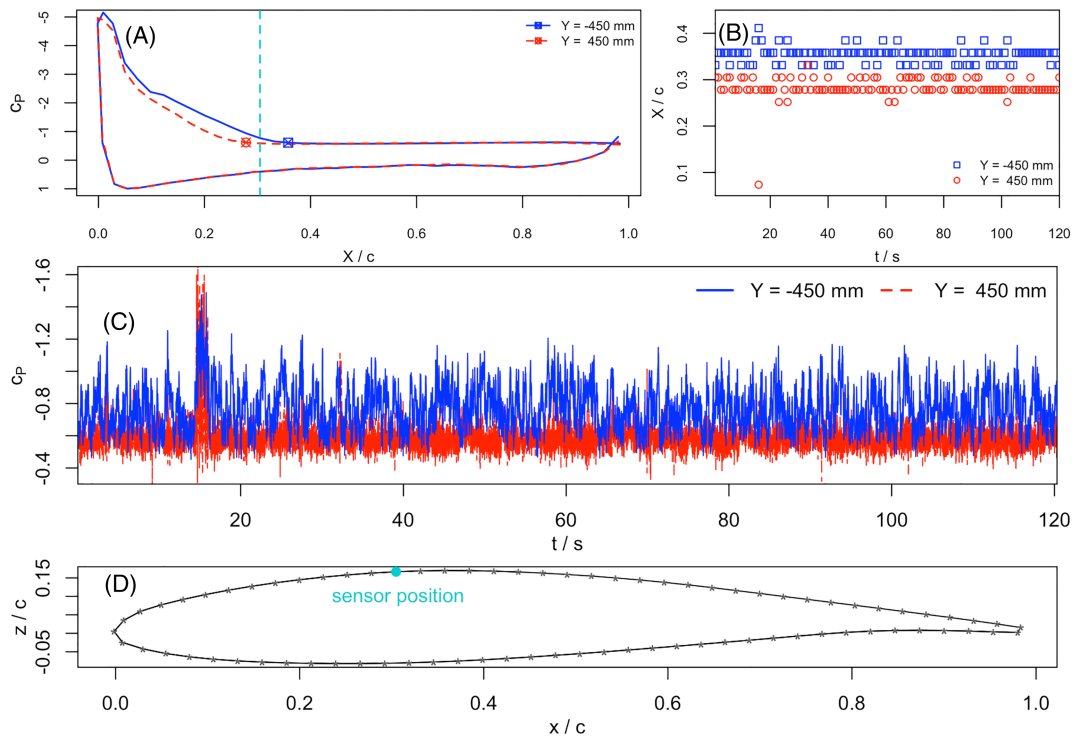


FIGURE 9 (A) Comparison of the c_p distributions at $\alpha = 24^\circ$ and $Re = 4.71 \cdot 10^6$ for the measurements at $Y_m = -450$ mm (blue line) and $Y_p = 450$ mm (red dashed line). The separation point is marked in addition for each curve. (B) Fluctuation of the separation point during the measurements. (C) Exemplary time series of a sensor (marked in D) located around the position of the separation point

4 | DISCUSSION AND CONCLUSION

In this work, we presented an aerodynamic investigation of a full-scale 2d wind turbine rotor blade section. At Reynolds number $Re = 4.7 \cdot 10^6$, experiments were compared to 2d URANS simulations used as a 2d reference case. Following the two research questions posed in the introduction, the analysis focused on the local and temporal instabilities present at angles of attack close to the maximum normal force. Thanks to the simultaneous acquisition of two rows of chord-wise pressure sensors at two span-wise locations we were able to observe a different behavior depending on the angle of attack. At $\alpha = 14^\circ$, the mean normal force becomes, despite the uniform inflow, asymmetric due to a trailing edge flow separation which occurs closer to the leading edge at the span-wise position Y_m than at Y_p . This asymmetry is found to be stable in time for this angle of attack. At $\alpha = 16^\circ$, the mean normal force is the same for both span-wise measurement positions, but the investigation of the instantaneous signals reveals a more complex behavior. A bi-stable level of the normal force is identified that was shown to reciprocally alternate both temporally and spatially. It was associated with sudden displacements of the separation points. The reciprocal alternations are correlated in space and time. This is observed for the first time as from the literature, nothing was indicating the existence of any coherence in the flow over the airfoil at high angles of attack where intermittent bursts in time and space were observed. From the literature, we do know that, once the flow separates, shear-layers develop (asymmetrically for asymmetric airfoils) on the upper and lower side of the blade, with coherent structures whose axes develop in the span-wise direction.²⁵ However, when the flow separation occurs at different chord-wise locations, it is not evident that the 2d shear layer structures are still linked in the span-wise direction. When increasing the angle of attack over 16° (see Figures 8 and 9), we show that this is actually not the case as the coherence of the pressure and lift drastically decreases between the span-wise lines. This study evidences a short range of angles of attack for which the flow separation location is highly unsteady and highly correlated in space and time, and more research will be needed.

Overall, the results indicate a high sensitivity of the flow around an airfoil at angles of attack close to the maximum normal force, including the presence of 3d effects at a 2d blade section in a uniform inflow. On the one hand, this could explain the strong variations in the results obtained in different wind tunnels in.¹⁵ On the other hand this shows the importance of thorough investigations of small effects that may trigger spontaneous attachment or detachment of the flow at these angles of attack. The flow separation is shown to be an extremely sensitive process, and a displacement of the separation point is associated with fluctuation of the lift force, and, thus, an increase in fatigue loads. Should the fluctuations be triggered on a real wind turbine, we are missing an important unsteady phenomenon in the blade design process and load evaluations. In addition, the fluctuations might be at the origin of additional source of noise.

With the current investigation, we are unable to connect any changes in the inflow to the instabilities that we observed both spatially and temporally. Therefore, further investigation of this phenomenon is needed to identify possible triggers. This is on the one hand important to improve experiments, moving towards temporally and spatially resolved measurements. On the other hand, in the future, it may help to avoid strong load variations at wind turbines in operation by understanding what triggers the unsteady behavior described here and controlling it to reduce loads.

ACKNOWLEDGEMENTS

This work was carried out within the research projects ASAPe with the funding from region Pays-de-Loire, Centrale Nantes, CSTB, and Ville de Nantes (Grant 2018 ASAPe), and ePARADISE with the funding from ADEME/region Pays-de-Loire (Grant 1905C0030). The authors would like to thank the West Atlantic Marine Energy Community (WEAMEC).

PEER REVIEW

The peer review history for this article is available at <https://publons.com/publon/10.1002/we.2732>.

DATA AVAILABILITY STATEMENT

Data available on request from the authors

ORCID

Ingrid Neunaber  <https://orcid.org/0000-0002-3787-3118>

REFERENCES

1. Vermeer LJ, Srensen JN, Crespo A. Wind turbine wake aerodynamics. *Progr Aerosp Sci*. 2003;39(6):467-510.
2. Boorsma K, Schepers JG. Rotor experiments in controlled conditions continued: New Mexico. In: *Journal of physics: Conference series*. IOP Publishing; 2016:753-2-022004.
3. Schaffarczyk AP, Schwab D, Breuer M. Experimental detection of laminar-turbulent transition on a rotating wind turbine blade in the free atmosphere. *Wind Energy*. 2017;20(2):211-220.
4. Madsen HA, Bak C, Schmidt Paulsen U, et al. The DAN-AERO MW experiments: final report. Risø-R-1726(EN), DTU; 2010.

5. Balaesque N, Bicker S, Dollinger C, et al. Investigations for improvement of energy yield of rotor-blades from the 1.5 MW class. In: *Journal of physics: Conference series* IOP Publishing; 2016:753-7-072012.
6. Krog Kruse E, Bak C, Olsen AS. Wind tunnel experiments on a NACA 63 3-418 airfoil with different types of leading edge roughness. *Wind Energy*. 2021.
7. Kerho MF, Bragg MB. Airfoil boundary-layer development and transition with large leading-edge roughness. *AIAA J*. 1997;35(1):75-84.
8. Sagol E, Reggio M, Ilinca A. Issues concerning roughness on wind turbine blades. *Renew Sustain Energy Rev*. 2013;23:514-525.
9. Akak S, Madsen HA, Srensen NN, Srensen JN, Fischer A, Bak C. Inflow turbulence and leading edge roughness effects on laminar-turbulent transition on naca 63-418 airfoil. *J Phys: Confer Ser*. 2018;1037(022005).
10. Manolesos M, Papadakis G. Investigation of the three-dimensional flow past a flatback wind turbine airfoil at high angles of attack. *Phys Fluids*. 2021; 33(8):85106.
11. Gault DE. A correlation of low-speed airfoil-section stalling characteristics with Reynolds number and airfoil geometry. Technical note 3963, National Advisory Committee for Aeronautics; 1957.
12. Li L, Hearst RJ. The influence of freestream turbulence on the temporal pressure distribution and lift of an airfoil. *J Wind Eng Ind Aerodyn*. 2021;209: 104456.
13. Devinant P, Laverne T, Hureau J. Experimental study of wind-turbine airfoil aerodynamics in high turbulence. *J Wind Eng Ind Aerodyn*. 2002;90: 689-707.
14. Sicot C, Aubrun S, Loyer S, Devinant P. Unsteady characteristics of the static stall of an airfoil subjected to freestream turbulence level up to 16%. *Exper Fluids*. 2006;41:641-648.
15. Olsen AS, Srensen NN, Bak C, Gaunaa M, Mikkelsen R, Fischer A, Beckerlee J, Ildvedsen S. Why is the measured maximum lift in wind tunnels dependent on the measurement method? *J Phys: Confer Ser*. 2020;1618(032040).
16. Bak C, Aagaard Madsen H, Fuglsang P, Rasmussen F. Observations and hypothesis of double stall. *Wind Energy*. 1999;2:195-2010.
17. Manolesos M, Papadakis G, Voutsinas SG. Experimental and computational analysis of stall cells on rectangular wings. *Wind Energy*. 2014;17:939-955.
18. Manolesos M, Voutsinas SG. Geometrical characterization of stall cells on rectangular wings. *Wind Energy*. 2014;17:1301-1314.
19. Ragni D, Ferreira C. Effects of 3d stall cells on the pressure distribution of a laminar naca wing. *Exper Fluids*. 2016;57:127.
20. Holmes JD, Lewis RE. The dynamic response of pressure-measurement systems. In: 9th Australasian Fluid Mechanics Conference; 1986; Auckland.
21. Whitmore SA, Petersen BJ, Scott DD. A dynamic response model for pressure sensors in continuum and high Knudsen number flows with large temperature gradients. Technical Memorandum 4728, NASA; 1996.
22. Rhie CM, Chow WL. A numerical study of the turbulent flow past an isolated aerofoil with trailing edge separation. *AIAA J*. 1983;17:1525-1532.
23. Issa RI. Solution of the implicitly discretised fluid flow equations by operator splitting. *J Comput Phys*. 1986;62:40-65.
24. Menter FR. Two-equation eddy viscosity turbulence models for engineering applications. *AIAA J*. 1994;32:1299-1310.
25. Thomareis N, Papadakis G. Effect of trailing edge shape on the separated flow characteristics around an airfoil at low Reynolds number: a numerical study. *Phys Fluids*. 2017;29:14101.

How to cite this article: Neunaber I, Danbon F, Soulier A, et al. Wind tunnel study on natural instability of the normal force on a full-scale wind turbine blade section at Reynolds number $4.7 \cdot 10^6$. *Wind Energy*. 2022;25(8):1332-1342. doi:[10.1002/we.2732](https://doi.org/10.1002/we.2732)